


Multiscale model of the physiological control of myocardial perfusion to delineate putative metabolic feedback mechanisms

Hamidreza Gharahi^{1,2}, C. Alberto Figueroa^{1,3}, Johnathan D. Tune⁴ and Daniel A. Beard² 

¹Section of Vascular Surgery, Department of Surgery, University of Michigan, Ann Arbor, MI, USA

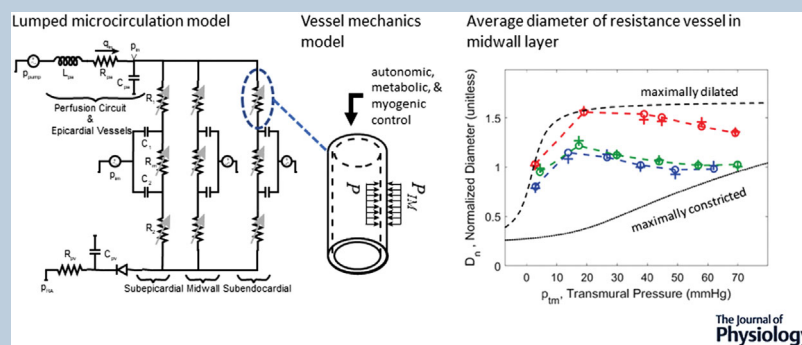
²Department of Molecular and Integrative Physiology, University of Michigan, Ann Arbor, MI, USA

³Department of Biomedical Engineering, University of Michigan, Ann Arbor, MI, USA

⁴Department of Physiology and Anatomy, University of North Texas Health Sciences Center, Fort Worth, TX, USA

Edited by: Bjorn Knollmann & Eleonora Grandi

The peer review history is available in the Supporting Information section of this article (<https://doi.org/10.1113/JP282237#support-information-section>).



Abstract Coronary blood flow is tightly regulated to ensure that myocardial oxygen delivery meets local metabolic demand via the concurrent action of myogenic, neural and metabolic mechanisms. Although several competing hypotheses exist, the specific nature of the local metabolic mechanism(s) remains poorly defined. To gain insights into the viability of putative metabolic feedback mechanisms and into the co-ordinated action of parallel regulatory mechanisms, we applied a multiscale modelling framework to analyse experimental data on coronary pressure, flow and myocardial oxygen delivery in the porcine heart *in vivo*. The modelling framework integrates a previously established lumped-parameter model of myocardial perfusion used to account for transmural haemodynamic variations and a simple vessel mechanics model used to simulate the vascular tone in each of three myocardial layers. Vascular tone in the resistance vessel mechanics model is governed by input stimuli from the myogenic, metabolic and autonomic control mechanisms. Seven competing formulations of the metabolic feedback mechanism are implemented in the modelling

Hamidreza Gharahi completed this study when he was a postdoctoral research fellow at University of Michigan, jointly working in Department of Molecular and Integrative Physiology and Department of Surgery-Section of Vascular Surgery. Prior to his postdoctoral training, he obtained a PhD in Mechanical Engineering from Michigan State University. Currently, he is a Senior Research Engineer at CFD Research Corporation. His research interests focus on mathematical modelling to understand the physiology and pathophysiology of coronary and pulmonary circulations.



This article was first published as a preprint. Gharahi H, Figueroa CR, Tune J, Beard DA. 2021. Multiscale model of the physiological control of myocardial perfusion to delineate putative metabolic feedback mechanisms. bioRxiv. <https://doi.org/10.1101/2021.08.04.455088>.

framework, and associated model simulations are compared with experimental data on coronary pressures and flows under a range of experimental conditions designed to interrogate the governing control mechanisms. Analysis identifies a maximally probable metabolic mechanism among the seven tested models, in which production of a metabolic signalling factor is proportional to myocardial oxygen consumption and delivery is proportional to flow. Finally, the identified model is validated based on comparisons of simulations with data on the myocardial perfusion response to conscious exercise that were not used for model identification.

(Received 6 August 2021; accepted after revision 31 January 2022; first published online 14 February 2022)

Corresponding author D. A. Beard: Department of Molecular and Integrative Physiology, University of Michigan, North Campus Research Center, 2800 Plymouth Road, B10-A122, Ann Arbor, MI 48109, USA. Email: beardda@umich.edu

Abstract figure legend A multi-scale model of coronary blood flow and myocardial perfusion is constructed from integrating: a lumped-parameter model of ventricular-vascular interaction in three transmural layers of the left-ventricular myocardium; and a model of resistance vessel mechanics accounting for regulation of smooth muscle tone by myogenic, autonomic, and metabolic mechanisms. The right panel shows model-predicted arterial resistance vessel diameter as a function of perfusion pressure under three different *in vivo* experimental conditions: control (blue); haemodilution (green); and haemodilution with dobutamine infusion (red).

Key points

- Although several competing hypotheses exist, we lack knowledge of specific nature of the metabolic mechanism(s) governing regional myocardial perfusion.
- Moreover, we lack an understanding of how parallel myogenic, adrenergic/autonomic and metabolic mechanisms work together to regulatory oxygen delivery in the beating heart.
- We have developed a multiscale modelling framework to test competing hypotheses against experimental data on coronary pressure, flow and myocardial oxygen delivery in the porcine heart *in vivo*.
- The analysis identifies a maximally probable metabolic mechanism among seven tested models, in which the production of a metabolic signalling factor is proportional to myocardial oxygen consumption and delivery is proportional to flow.

Introduction

The left ventricular myocardium extracts ~70–80% of the oxygen delivered from the arterial blood under normal resting conditions. A consequence of this high degree of myocardial oxygen extraction is that increases in myocardial oxygen demand (such as during exercise) require proportionate increases in perfusion to the myocardium to maintain adequate tissue oxygenation. This tight coupling of myocardial oxygen delivery with metabolism is observed to occur not only during physiological increases in myocardial oxygen consumption ($M\dot{V}_{O_2}$), but also following perturbations to coronary perfusion pressure (CPP), which are crucial, especially in response to proximal stenotic lesions of epicardial coronary arteries.

Our understanding of the mechanisms underlying the balance between coronary blood flow and $M\dot{V}_{O_2}$ remains limited. Putatively, coronary flow regulation is mediated via the concurrent action of three major control mechanisms: (1) a myogenic mechanism where resistance arterioles constrict in response to increases in vascular wall tension; (2) an autonomic mechanism

were stimulation of β -receptors on arterial smooth muscle leads to vasodilatation; and (3) a metabolic mechanism where an increase in $M\dot{V}_{O_2}$ promotes local vasodilatation. These mechanisms work in parallel and converge on common end-effector pathways of coronary microvascular resistance (i.e. vascular smooth muscle tone). Moreover, the actions of these control mechanisms are influenced by structural and contractile properties of the myocardium and vary transmurally across layers of the myocardium (Bassingthwaight *et al.* 2001). Precisely how these purported mechanisms work together dynamically and regionally, in the beating heart where cardiac contraction causes a constricting force on the vessels in the walls of the heart, impeding flow, particularly in the subendocardium, during systole, merits further investigation. Furthermore, although several competing hypotheses exist, the specific nature of local metabolic mechanism(s) remains poorly defined.

The paradigm of local metabolic control of coronary blood flow centres around the hypothesis that vasoactive metabolites are produced in proportion to the

prevailing level of myocardial oxygenation. This hypothesis is attractive in that it provides a mechanism directly linking increases in metabolism and reductions in tissue oxygen tension (typically indexed by coronary venous P_{O_2}) with commensurate changes in coronary blood flow (Dole & Nuno, 1986). However, this general framework offers little insight into if or how specific metabolites (e.g. adenosine and NO) or pathways (e.g. end-effector K^+ channels) contribute to myocardial oxygen supply/demand balance. In addition, prior observations that coronary venous P_{O_2} does not directly correlate with changes in coronary blood flow during increases in $M\dot{V}_{O_2}$ (Duncker & Bache, 2008; Tune *et al.* 2020) or perturbations in CPP (Kiel *et al.* 2018) fail to support the metabolic hypothesis as proposed. Thus, both the general framework and the specific molecular signals involved in the local metabolic control of coronary blood flow continues to linger as one of the highly (if not the most) contested mysteries of the coronary circulation.

The present study aimed to address these knowledge deficits through model-based analysis of experimental data on *in vivo* coronary flow regulation in response to changes in perfusion pressure, $M\dot{V}_{O_2}$ and the oxygen carrying capacity of the blood. Specifically, a multiscale model of coronary flow regulation was constructed to account for putative myogenic, neural and metabolic mechanisms, as well as transmural dynamics of blood circulation and ventricular-vascular interactions. Model simulations were compared with data on coronary flow and zero-flow coronary pressure recordings obtained distal to epicardial occlusions *in vivo* in pigs (Kiel *et al.* 2018) and subendocardial-to-subepicardial flow ratio. Coronary flow and zero-flow pressure transients were obtained over a range of initial perfusion pressures and under control conditions, as well as for haemodilution and haemodilution with dobutamine infusion.

The model used to analyse these data is built based on the lumped three-layer model of myocardial perfusion (Mynard *et al.* 2014) and the myogenic autoregulatory vessel model of Carlson & Secomb (2005), with additional components representing β -mediated vasodilatation and a metabolic feedback mechanism. Several competing representations of the metabolic mechanism were implemented and tested against the data. Using maximal-likelihood structural and parametric model identification to rule out and refine hypotheses, we identify a novel formulation of the metabolic mechanism in which the metabolic signal is represented as proportional to metabolic rate and flow. This mechanism can be interpreted as representing an ephemeral metabolic signal for which production is proportional to $M\dot{V}_{O_2}$ and delivery is proportional to flow. Potential candidates for such a signal include short-lived reactive species such as H_2O_2 (Saitoh *et al.* 2006). The identified model is further validated based on

comparisons of simulations with data on the myocardial perfusion response to conscious exercise that were not used for model identification.

Methods

Experimental data for model identification and validation

Experimental data for model identification were obtained from prior studies on coronary blood flow autoregulation, including measurements of distal pressure transients in the left-anterior descending (LAD) arterial tree following proximal occlusion of the main LAD trunk in anaesthetized pigs. The experimental details are described in Kiel *et al.* (2018). In brief, for a given experimental condition, the LAD artery was initially perfused at a constant baseline pressure by a servo-controlled pump. After a steady baseline, flow at a given perfusion pressure was attained, the LAD trunk was occluded and the resulting decay in arterial pressure at a distal epicardial location was measured. The aortic pressure was continuously measured throughout the experiment via a femoral artery catheter. In addition, arterial and venous blood samples were collected to measure blood oxygenation and haematocrit.

Example pressure transients obtained under control conditions (without dobutamine infusion or haemodilution) are illustrated in Fig. 1A. In these data sets, each of the six subpanels in Fig. 1A corresponds to a different average initial perfusion pressure, ranging from 40 to 140 mmHg. The perfusion pressure oscillated around the set CPP level in sync with the measured arterial pressure. The upstream occlusion is induced at approximate time $t = 7$ s, resulting in a decay in pressure as blood drains from the arterial tree. The pressure oscillations, associated with myocardial contraction, continue during the decay. The final pressure attained after the ~ 4 s transient decay is denoted the zero-flow pressure, P_{zf} , which is used as a metric of myocardial resistance vessel tone. In our analysis, we match model simulations to the full time course of the zero-flow pressure experiment, as illustrated in Fig. 1.

Experiments from Kiel *et al.* (2018) also provide data on total flow (before occlusion) at each level of initial perfusion pressure, as illustrated in Fig. 1B for the baseline experimental condition for an individual animal. Finally, our model identification is constrained to match the experimentally measured baseline subendocardial-to-subepicardial flow ratio (ENDO/EPI), as illustrated in Fig. 1C.

The zero-flow pressure experiment was repeated under three different experimental conditions: (1) control; (2) haemodilution; and (3) haemodilution + dobutamine. Haemodilution was induced by gradually replacing equal

volumes of blood with a synthetic plasma expander. Dobutamine was administered by an i.v. drip to increase heart rate to ~ 75 – 100% above baseline levels.

Additional experimental data on conscious animals are used for validation. Briefly, animals were chronically instrumented with an arterial catheter, a perivascular flow transducer around the left anterior descending coronary artery and a solid state pressure transducer in the left ventricle as described previously (Berwick *et al.* 2012). Following recovery from surgery, haemodynamic variables were continuously measured under baseline resting conditions and subsequently during treadmill exercise.

Overview of model formulation

Coronary blood flow regulation is simulated by integrating a lumped model for myocardial perfusion in the subendocardial, midwall and subepicardial layers of the myocardium (Model 1) with a model of resistance vessel mechanics accounting for myogenic, autonomic and metabolic regulatory mechanisms (Model 2). In practice, the integrated model is identified in a two-step process. First, the lumped model is fit to data from zero-flow pressure experiments, yielding estimates of vessel diameters as functions of transmural pressure in the different myocardial layers under different levels of perfusion pressure and oxygen demand, at different

heart rates and under different experimental conditions. Next, the vessel mechanics model (Model 2) identified by comparing a panel of model formulations representing competing hypotheses for the metabolic mechanism with estimated diameters obtained from Model 1. Finally, the identified vessel mechanics model is validated by combining the two models to simulate myocardial blood flow in exercise vs. baseline resting conditions.

Three-layer lumped model of myocardial perfusion (Model 1)

To simulate myocardial perfusion, we adapt the lumped model developed by Spaan *et al.* (2000), Mynard *et al.* (2014) and Mynard & Smolich, 2016), as illustrated in Fig. 2. For the zero-flow pressure experiments, this model is used to simulate constant-pressure blood flow to the myocardium driven to the LAD artery by the extracorporeal servo-controlled pump and the zero-flow pressure decay transient. The hydraulic properties of the perfusion tubing and epicardial vessels are governed by a series lumped resistance, blood inertance and compliance, as illustrated in Fig. 2. A venous resistance and compliance drain into the right-atrial pressure (P_{RA}) downstream of a valve that prevents backflow in low perfusion pressures (Ho *et al.* 2004). The myocardial circulation is divided into three parallel circuits representing the sub-epicardial, midwall and subendocardial layers. Within

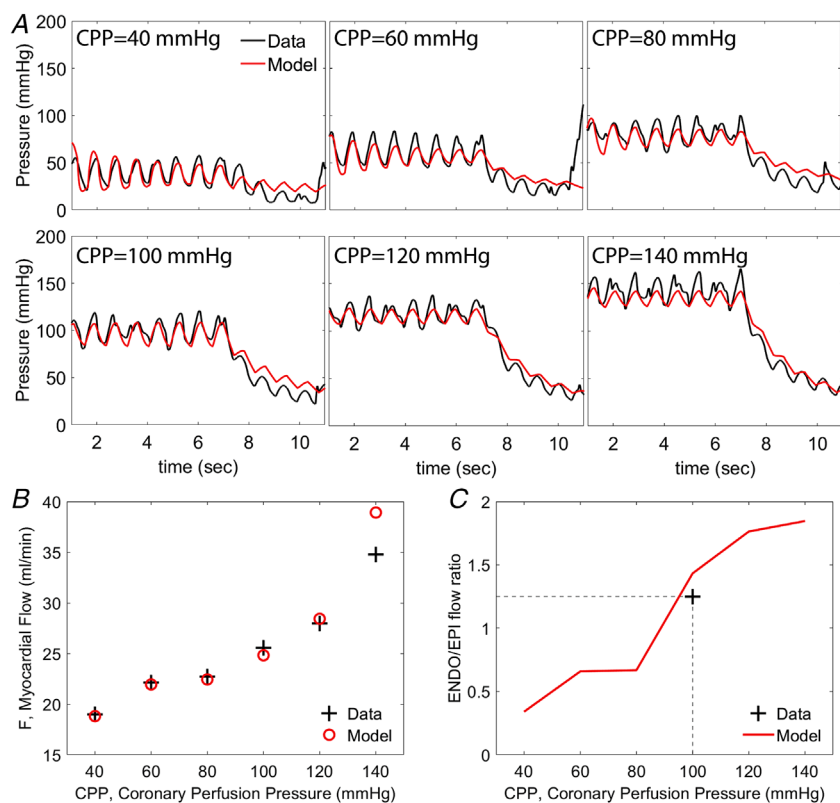


Figure 1. An example data set used to identify Model 1 for an individual animal under control conditions

A, pressure recordings obtained at six levels of CPP following occlusion of the LAD artery. The artery is occluded at ~ 7 s and the decay distal to the occlusion is recorded. B, total LAD flow, measured at different values of CPP. C, myocardial subendocardial-to-subepicardial (ENDO/EPI) flow ratio before the occlusion. Data in (A) and (B) are from Kiel *et al.* (2018). Measured ENDO/EPI flow ratio under baseline control conditions is targeted to 1.25 (for details, see text). Measured data are plotted in black; model simulations are in red. [Colour figure can be viewed at wileyonlinelibrary.com]

each layer, three serial resistances represent arterial, capillary and venous compartments. Using the Poiseuille resistance–volume relationship, the arterial ($i = 1$) and venous ($i = 2$) resistances (R_1 and R_2 in Fig. 2) are computed:

$$R_{ij}(t) = R_{0,i} \left(\frac{V_{0,ij}}{V_{ij}(t)} \right)^2, \quad i \in \{1, 2\}, \quad j \in \{1, 2, 3\} \quad (1)$$

where $R_{0,i}$ and $V_{0,i}$ are reference resistance and volume, respectively, and the index j denotes myocardial layer: (1: subepicardial, 2: midwall and 3: subendocardial). This resistance–volume relationship represents a major simplifying assumption of the model, where it is assumed that two representative lumped resistances govern conductivity to a given layer. Equivalently, this assumption implies that: (1) perturbations in total microvascular blood volume are allocated throughout the elements of the microvascular network in proportion to the volume in those elements; (2) the radii of all resistance vessels in the microcirculation are proportional to the square roots of the volume of blood in those vessels; and (3) the pressure drops across these vessels is inversely proportional to the radius of vessel diameter.

The instantaneous volume V_{ij} (volume of compartment i in layer j) is computed as:

$$V_{ij}(t) = \max(V_0 + C_{ij}P_{tm,ij}(t), V_c) \quad (2)$$

where transmural pressure ($P_{tm,ij}$) is the difference between to blood pressure (P) and the intramyocardial

pressure ($P_{im,j}$) (Mynard *et al.* 2014). Based on the analysis in Mynard *et al.* (2014), we assume:

$$P_{im,j} = 1.2d_j P_{lv} \quad (3)$$

where d_j is the relative depth of subendocardial ($d_j = \frac{5}{6}$), midwall ($d_j = \frac{1}{2}$) and subepicardial layers ($d_j = \frac{1}{6}$). To estimate P_{lv} , we use half-sine functions constrained to match the measured aortic pressure where $P_{lv} = p_{ao}$ in the systolic phase and $P_{lv} = 5$ mmHg in the diastolic phase. An example estimated ventricular pressure time course and corresponding measured aortic pressure time course are illustrated in the Supporting information (Fig. S1).

This model formulation allows for a potential collapse of vessels in cases of largely negative transmural pressures. This collapse is prevalent in the subendocardial layer and is characterized with a transmural pressure below which the vascular volume remains almost constant (V_c) (Hoffman & Spaan, 1990; Kiel *et al.* 2018). Following Guiot *et al.* (1990), we assume that the laminar flow assumptions for the un-collapsed vessel (Eqn. 1) are effectively valid for collapsed vessels.

Lastly, the middle resistance R_{mj} in each layer is computed using the resistance of the arterial and venous compartments

$$R_{mj}(t) = \gamma R_{1j}(t) + (1 - \gamma) R_{2j}(t) \quad (4)$$

where γ is a parameter between 0 and 1. To ensure a physiologically realistic transmural flow, the reference resistance $R_{0,1}$ and the arterial compliances C_{1j} are

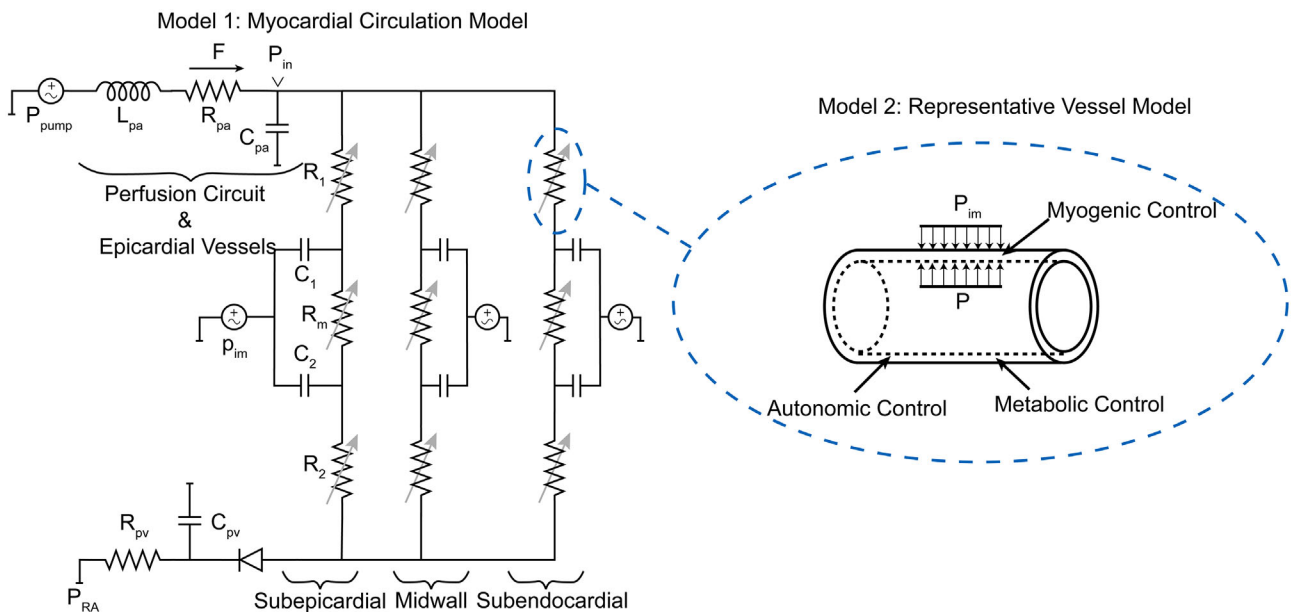


Figure 2. Schematic of the modelling approaches
 Model 1: the myocardial circulation model which determines the flow and pressure in each layer of the myocardium.
 Model 2: a representative vessel model endowed with regulatory mechanisms to determine the level of vascular tone in each layer. [Colour figure can be viewed at wileyonlinelibrary.com]

scaled with two factors: subepicardial to subendocardial resistance factor r_f and compliance factor c_f .

To simulate changes in vascular tone (dilatation/constriction) in response to changes in CPP in the lumped model, a vasoreactivity factor f_j is defined such that:

$$C_{1j} = f_j \times C_{ij}^0 \quad (5)$$

where $f_j > 1$ represents vasodilatation, $f_j < 1$ represents vasoconstriction and C_{ij}^0 is a reference value corresponding to the baseline conditions taken to be CPP = 100 mmHg. The vasoreactivity factor is assumed to vary across different across the myocardium. To incorporate graded vasoreactivity, a parameter $0 < \beta < 1$ is introduced such that:

$$\begin{aligned} f_1 &= f_{CPP} - \beta (f_{CPP} - 1) \\ f_2 &= f_{CPP} \\ f_3 &= f_{CPP} + \beta (f_{CPP} - 1) \end{aligned} \quad (6)$$

where f_{CPP} is the overall vasoreactivity factor.

To simulate the zero-flow pressure experiment, we divide the experiment to two parts: part 1 when the pump is driving flow to the LAD perfusion region and part 2 when the pump is off and the extracorporeal circuit is clamped. To simulate first part of the experiment, we assume that the output pressure from the pump is constant and set to the nominal CPP for simulation time $0 < t < t_{\text{off}}$, where t_{off} is when the pump is turned off and the extracorporeal circuit is clamped. For this first part of the experiment, the fixed driving pressure is used to drive the model and the resulting simulated flow is compared with the measured data.

To simulate the second part of the experiment, flow is imposed and the resulting pressure transient is simulated. Specifically, because the model cannot accommodate a step change in flow, a rapid continuous decrease to zero flow is imposed using the function:

$$F(t) = F(t_{\text{off}}) e^{-\alpha(t-t_{\text{off}})}, t > t_{\text{off}} \quad (7)$$

The rate of decay is set to the value $\alpha = 10 \text{ s}^{-1}$ to obtain a decay to zero flow that is effectively instantaneous compared to the time scale of the observed pressure decay.

Parameter estimation for Model 1. Phasic tracings of perfusion pressure and flow for each experimental preparation are used to calibrate the myocardial circulation model. The perfusion pressure is measured continuously in both steps of the experiment using a cannula in the LAD coronary artery in both steps of the experiment. Accordingly, in our model, the pressure measurements

correspond to P_{in} in Fig. 2. The model residual vector is defined as:

$$r_p(t_k) = \frac{P_{in}(t_k) - P_{in}^{data}(t_k)}{P_{in}^{data}(t_k)} \quad (8)$$

where P_{in}^{data} is the measured data at time t_k . The flow across R_{pa} , q_{in} , is compared with the measured flow. As a result of pump-induced noise in flow tracings, the average flow before closing the circuit (\bar{F}) is used in the objective:

$$r_q = \frac{\bar{F} - \bar{F}_{data}}{\bar{F}_{data}} \quad (9)$$

where \bar{F}_{data} the average of flow before the extracorporeal circuit is clamped. The cost function for the parameter estimation is a weighted sum of the error in time-resolved pressure tracings, average flow before clamping the perfusion circuit and a penalty term to ensure a physiological subendocardial to subepicardial flow ratio (ENDO/EPI) for each CPP level:

$$E_{CPP} = w_1 r_p^T r_p + w_2 r_q^2 + w_3 (ENDO/EPI - 1.25) \quad (10)$$

The weights w_1 and w_2 are chosen such that the contribution of the pressure and flow to the cost function are the same order. The weight w_3 is varied for CPP levels, assuming the largest weight for the CPP = 100 mmHg case, where the target ENDO/EPI ratio at rest is 1.25, reflecting the approximate average of values previously reported in the literature (Breisch *et al.* 1986a,b; Krombach *et al.* 1999). Finally, the total cost function for parameter estimation can be written as:

$$E_1 = \sum_{CPP} E_{CPP} \quad (11)$$

In the present study, the model parameters corresponding to the venous components of the model were fixed, and the arterial component parameters were adjusted to minimize the objective function E_1 . Table 1 lists the adjustable parameters and their description.

Representative vessel model (Model 2)

In the representative vessel model, the arterial component in each layer is represented by a single vessel endowed with passive and active tension models, as well as myogenic, metabolic and autonomic regulatory mechanisms. Following Carlson & Secomb (2005) and Carlson *et al.* (2008), the vessel wall tension is sum of a passive tension T_{pass} and an active tension T_{act} , which is the tension generated by the vascular smooth muscle cells (VSMs). The active tension is determined as the product of the maximal active tension T_{act}^{max} in a given vessel and the

Table 1. List of adjusted parameters for Model 1

| Parameter | Mean (range) of estimated values | Unit | Description |
|-----------|---|--|--|
| L_{pa} | 1.737 (0.129–3.976) | mmHg (mL s ⁻²) ⁻¹ | Blood inertance in perfusion circuit and epicardial vessels |
| R_{pa} | 2.729 (0.367–8.511) | mmHg (mL s ⁻¹) ⁻¹ | Resistance in perfusion circuit and epicardial vessels |
| C_{pa} | 0.0211 (0.009–0.042) | mL mmHg ⁻¹ | Compliance in perfusion circuit and epicardial vessels |
| V_0 | 0.455 (0.218–0.643) | mL | Reference volume |
| V_c | 0.194 (0.020–0.599) | mL | Collapsible volume |
| $R_{0,3}$ | 104.00 (46.33–217.43) | mmHg (mL s ⁻¹) ⁻¹ | Reference subendocardial arterial resistance |
| C_{13} | 0.0044 (0.001–0.010) | mL mmHg ⁻¹ | Subendocardial arterial compliance |
| c_f | 0.8686 (0.716–0.999) | – | The ratio of subepicardial to subendocardial compliance |
| r_f | 1.4549 (2.047–1.006) | – | The ratio of subepicardial to subendocardial resistance |
| β | 0.3360 (0.034–0.819) | – | Degree of graded vasoreactivity |
| f_{CPP} | [7.43 (1.006–19.522), 7.11 (2.015–12.183), 2.55 (1.163–6.221), 0.38 (0.002–0.999) and 0.30 (0.003–0.999)] | – | Vasoreactivity factor for CPP = 40, 60, 80, 120 and 140 mmHg |

activation level A . Thus, the vascular tension can be written as:

$$T = T_{pass} + A T_{act}^{max} \tag{12}$$

The passive response of the vessel is expressed as a non-linear function of diameter, by rearranging the non-linear pressure–diameter relationship in Young *et al.* (2012):

$$T_{pass} = \frac{D}{2} \left(\phi_p + C_p \tan \left(\frac{\pi \left(\frac{D}{2} - B_p \right)}{A_p - B_p} - \frac{\pi}{2} \right) \right) \tag{13}$$

where A_p and B_p represent the asymptomatic maximum and minimum radii, C_p is the bandwidth between A_p and B_p , and ϕ_p corresponds to the pressure offset determining the half-way point between A_p and B_p . The maximal active tension generated by VSM is expressed by modifying the Gaussian function given in Carlson & Secomb (2005) so that the maximal possible active tension diminishes for small diameters:

$$T_{act}^{max} = \frac{\rho_m D}{2 \exp \left(-C_m \left(\frac{D}{2} - \phi_m \right)^2 \right)} \tag{14}$$

Following Carlson *et al.* (2008), the activation level A depends on the total stimulus S_{tone} in a sigmoidal manner:

$$A = \frac{1}{1 + \exp(-S_{tone})} \tag{15}$$

where S_{tone} is a net summation of stimuli from the myogenic S_{myo} , metabolic S_{meta} and autonomic S_{HR} mechanisms, and an offset C_0 :

$$S_{tone} = S_{myo} + S_{HR} + S_{meta} + C_0 \tag{16}$$

We assume myogenic response is a linear function of the vascular tension, so we can write:

$$S_{myo} = C_{myo} T \tag{17}$$

The autonomic response is assumed to be a function of the heart rate and to have only dilatory effects on the myocardial vessels. Moreover, a baseline offset HR_0 is used to determine the threshold for autonomic signal generation:

$$S_{HR} = -C_{HR} \max(HR - HR_0, 0) \tag{18}$$

Similarly for metabolic mechanism, we assume the stimuli linearly depends on the signal:

$$S_{meta} = -C_{meta} MS \tag{19}$$

where MS is the metabolic signal, and the negative sign corresponds to a vasodilatory response.

In the present study, we evaluated seven different representations of the metabolic signal:

- (1) *ATP-dependent (ATP)*: ATP release from red blood cells provides the metabolic feedback signal for local control of perfusion. The ATP transport

model of Pradhan *et al.* (2016) accounts for oxygen saturation-dependent leak of ATP from red blood cells and a flow-dependent washout of ATP from the circulation. From Pradhan *et al.* (2016), the metabolic signal is assumed proportional to venous ATP, which is governed by:

$$MS_{atp} = [ATP]_v = [ATP]_a + \frac{V_{cap}HctJ_0S_0}{LVw(S_a - S_v)} e^{\frac{S_a}{S_0}} \left[e^{\frac{S_a - S_v}{S_0}} - 1 \right] \quad (20)$$

where $[ATP]_v$ and $[ATP]_a$ are arterial and venous plasma ATP concentrations, V_{cap} is the capillary volume density, LVw is the left ventricle weight, J_0 is the ATP release rate in coronary vascular bed and S_0 is the ATP release parameter of the model. The main assumptions of this model are: (1) the rate of ATP release into plasma decreases exponentially with RBC O_2 saturation and is proportional to Hct and (2) the ATP-dependent signal does not degrade across myocardial circulation.

- (2) *Myocardial oxygen consumption* ($M\dot{V}_{O_2}$): Myocardial oxygen consumption determines the metabolic signal. Under given experimental conditions, total $M\dot{V}_{O_2}$ is approximated:

$$MVO_2 = \frac{\bar{F}}{LVw} \times (CaO_2 - CvO_2) \quad (21)$$

where CaO_2 and CvO_2 are the arterial and venous oxygen content. Experimental studies have shown that that myocardial fibre shortening and energy demands in subendocardium are higher than those of subepicardium (Holtz *et al.* 1977). This leads to variable oxygen consumption levels across the myocardium, with subendocardial to subepicardial $M\dot{V}_{O_2}$ ratio (R_M) of ~ 1.5 (Holtz *et al.* 1977; Vinten-Johansen & Weiss, 1980). Based on these observations, we assume a constant R_M and thus the layer-wise $M\dot{V}_{O_2}$ is computed by dividing $M\dot{V}_{O_2}$:

$$MS_{MVO_2} = \begin{cases} MVO_{2subendo} = MVO_2 \frac{2}{3} \frac{R_M}{R_M + 1} \\ MVO_{2subepi} = MVO_2 \frac{2}{3} \frac{1}{R_M + 1} \\ MVO_{2midwall} = \frac{1}{2} (MVO_{2subendo} + MVO_{2subendo}) \end{cases} \quad (22)$$

- (3) *Oxygen extraction* ($S_a - S_v$): The arterial-venous difference in oxygen saturation acts as a signal for metabolic control. Assuming the oxygen extraction is uniform across the layers, the metabolic signal is expressed as:

$$MS_{EX} = S_a - S_v \quad (23)$$

- (4) *Layer-wise variable oxygen extraction* (LS_v): The regional arterial-venous difference in oxygen saturation acts as a signal for metabolic control. Using the layer-wise $M\dot{V}_{O_2}$ (metabolic signal #2), we compute venous oxygen saturation and arterial-venous oxygen extraction in each of three layers of the myocardium:

$$S_{vj} = S_a - \frac{MVO_{2j}}{\frac{\bar{F}_j}{LVw} \cdot c_0 \cdot Hct}, \text{ for } j \in \{\text{subendo.}, \text{midwall}, \text{subepi.}\}, MS_{LSv} = S_a - S_{vj} \quad (24)$$

where c_0 is the oxygen content of fully oxygen saturated oxyhaemoglobin in a red blood cell.

- (5) *Flow times oxygen extraction* ($F\Delta S$): The metabolic signal is the product of flow and oxygen extraction in each layer of the myocardium:

$$MS_{Q\Delta S} = F_j (S_a - S_{vj}), \text{ for } j \in \{\text{subendo.}, \text{midwall}, \text{subepi.}\} \quad (25)$$

- (6) *Flow times $M\dot{V}_{O_2}$* (FM): The metabolic signal is the product of flow and $M\dot{V}_{O_2}$ in each layer of the myocardium:

$$MS_{FM} = F_j MVO_{2j}, \text{ for } j \in \{\text{subendo.}, \text{midwall}, \text{subepi.}\} \quad (26)$$

In metabolic signals 5 and 6, similar to metabolic signals 2 and 4, the layer-wise oxygen extraction is computed assuming a constant R_M .

- (7) *Oxygen consumption squared* ($M\dot{V}_{O_2}^2$): Because the calculation of $M\dot{V}_{O_2}$ from experimental measurements of oxygen extraction depends on flow (eqn. 22), metabolic signal 6 is proportional to F_j^2 and oxygen extraction ($CaO_2 - CvO_2$). As a final candidate, we assume metabolic signal 6 to be proportional to the squares of both flow and oxygen extraction. Accordingly, the metabolic signal is written as the square of the myocardial oxygen consumption rate:

$$MS_{MVO_2^2} = (MS_{MVO_2})^2 \quad (27)$$

Parameter estimation for Model 2. Outputs of the parameterized Model 1, fit to data from the zero-flow pressure experiments, are used to estimate the layer-wise average diameters of representative resistance vessels, \bar{D}_j , for each experimental condition (control, haemodilution and haemodilution + dobutamine), each level of CPP, in each layer of the myocardium, and for each of four experimental animals. Additional inputs to Model 2 are average haemodynamics (pressure and flow) and

estimated tissue pressures in each layer of the myocardium, blood oxygenation measurements and heart rate.

The layer-wise flow \bar{F}_j , transmural pressure $P_{tm,j}$ and resistance \bar{R}_j are computed from the cycle-to-cycle averaged results of Model 1 for each experimental condition and each animal. The estimated Model 1 resistances \bar{R}_i of the arterial components are used to determine representative vessel diameters:

$$\bar{D}_j = 100 \cdot \left(\frac{\bar{R}|_{\text{control, midwall, CPP}=100}}{\bar{R}_j} \cdot \frac{\mu}{\mu|_{\text{control, CPP}=100}} \right)^{\frac{1}{4}} \tag{28}$$

where the diameter of midwall at CPP = 100 mmHg level is assumed to be 100 μm . The effective blood viscosity μ is determined as a function of haematocrit using the relationship (Snyder, 1971):

$$\mu = 2.03 \cdot \exp \left[(0.0322 - 1.08e - 4 \cdot \text{Temp}) \cdot \text{Hct} - 0.02 \cdot \text{Temp} \right] \tag{29}$$

where *Hct* and *Temp* are haematocrit and temperature, respectively.

Figure 3A shows how the estimated representative vessel diameter varies with transmural pressure in the midwall layer of an individual animal for the three different experimental conditions. To match the predictions of the vessel model (Model 2) with these

estimated diameters, the following objective function is used for parameter estimation:

$$E_2 = \left\| \bar{\mathbf{D}}_j^{\text{Model 2}} - \bar{\mathbf{D}}_j^{\text{Model 1}} \right\| \tag{30}$$

where $\bar{\mathbf{D}}_j^{\text{Model 1}} = [\bar{D}_j^{\text{control}}, \bar{D}_j^{\text{anaemia}}, \bar{D}_j^{\text{anaemia+dobutamine}}]$ is the vector of computed diameters representing the same pig/same layer, and $\bar{\mathbf{D}}_j^{\text{Model 2}}$ is the corresponding Model 2 predictions. The adjustable parameters are listed in Table 2.

Model 2 model selection. The parameter estimation is repeated using each of the seven different metabolic signal models. To compare the performance of each model formulation, we use a modified second order Akaike information criterion (*AICc*), which is used for model selection across multiple datasets with small sample size (Navakatikyan, 2007; Vinnakota *et al.* 2010)

$$AICc = \sum_{i=1}^N \left(n_i \cdot \ln \left(\frac{RSS}{n_i} \right) \right) + 2KN \left(\frac{n_t}{n_t - KN - N} \right) \tag{31}$$

where *RSS* is the residual sum of squares ($RSS = E_2^2$), *K* is the number of parameters, *N* is the number of data sets (4 pigs \times 3 layers = 12 datasets) and n_i is the number of data points in each data set (Fig 1: 15, Fig 2: 12, Fig 3: 18, Fig 4:

Figure 3. Vasoregulation as a function of transmural wall pressure
 A, model predictions of relative resistance vessel diameters are shown for the midwall layer for pig C for the midwall layer. Diameters for the three experimental conditions, associated with the fits of Model 1 to the zero-flow pressure experiment, are plotted as '+' markers: blue for control; green for haemodilution; and red for haemodilution + dobutamine. The matches of Model 2-based predictions (using the *FM*, flow times $M\dot{V}_{O_2}$, metabolic signal) to the diameter estimates are plotted as 'o' markers connected by dashed lines. B, predicted total smooth muscle activation is plotted as a function of transmural pressure in the zero-flow pressure experiment. C, predicted myogenic activation signal is plotted as a function of transmural pressure in the zero-flow pressure experiment. D, predicted autonomic activation signal is plotted as a function of transmural pressure in the zero-flow pressure experiment. E, predicted metabolic activation signal is plotted as a function of transmural pressure in the zero-flow pressure experiment. [Colour figure can be viewed at wileyonlinelibrary.com]

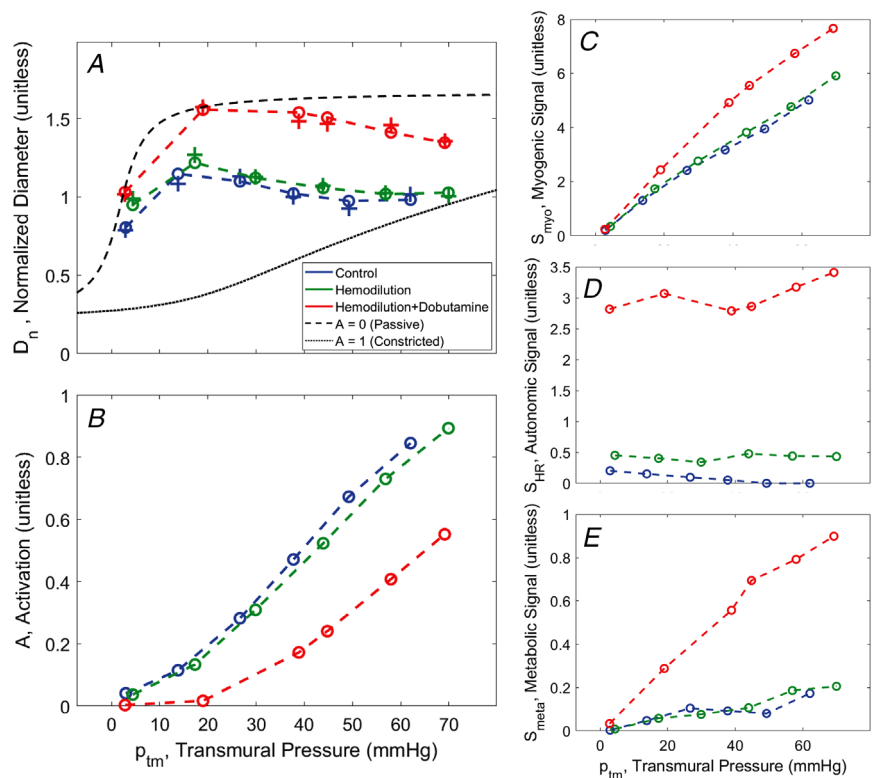


Table 2. List of adjustable parameters for Model 2

| Parameter | Subepicardial* | Midwall* | Subendocardial* | Unit | Description |
|------------|----------------|----------|-----------------|--------------------|---|
| A_p | 103.639 | 88.173 | 91.765 | – | Maximum asymptotic radius |
| B_p | 12.653 | 17.925 | 19.225 | – | Minimum asymptotic radius |
| C_p | 13.310 | 4.171 | 30.677 | mmHg | Bandwidth between A_p and B_p |
| ϕ_p | 2.212 | –5.933 | –14.544 | mmHg | Pressure offset |
| ρ_m | 344.551 | 302.345 | 164.330 | mmHg | Magnitude of active tension |
| C_m | 86.355 | 77.231 | 133.991 | – | Spread of Gaussian |
| ϕ_m | 142.857 | 126.668 | 112.545 | – | Centre of Gaussian |
| C_{myo} | 22.554 | 11.446 | 10.776 | mmHg ⁻¹ | Myogenic coefficient |
| C_{HR} | 0.026 | 0.034 | 0.081 | min | Autonomic coefficient |
| HR_0 | 92.302 | 79.642 | 75.657 | min ⁻¹ | Heart rate offset |
| C_{meta} | 0.467 | 0.196 | 0.195 | [Model dependent] | Metabolic coefficient |
| S_0 | 0.0157 | 0.0100 | 0.0133 | – | ATP release parameter (only for ATP-dependent case) |
| C_0 | –6.351 | –2.429 | –0.752 | – | Tone offset |

*Mean parameter estimate listed for the top-ranked model, except for S_0 , which is a parameter only for the ATP-dependent model.

18) and n_t is the total number of data points (63). Then, a parameter Δ for each is computed as:

$$\Delta_k = AICc_k - AICc_{min} \quad (32)$$

where $AICc_k$ is the Akaike criterion for k^{th} model and $AICc_{min}$ is the minimum $AICc$ value. Finally, the relative likelihood (RL_i), is given by:

$$RL_k = \exp(-0.5\Delta_k) \quad (33)$$

which is the probability that a particular k^{th} model is a better model than the model with the minimum $AICc$ value.

A genetic algorithm is used for the parameter estimation in both models. For Model 1 parameters, a population size of 600 and number of generations 1200 was used, although the procedure converged before reaching the 1200 generations in all cases. For Model 2 parameters, we fixed the population size and number of generations to 1000 and 10000, respectively. For both models, the cross-over and mutation probabilities were fixed to 0.8 and 0.01, respectively, and the convergence tolerance was 10^{-8} . The last generation was evaluated in each case to ensure unique results.

Simulating coronary flow in rest vs. exercise conditions

Once the coronary flow regulation model is constructed, the identified model framework, with Models 1 and 2 integrated together, is validated by simulating *in vivo* myocardial perfusion in resting and exercise conditions. These simulations are compared with data collected in conscious animals, for which aortic and left ventricular pressure and LAD flow were simultaneously measured.

The measured aortic pressure was used to drive the model and simulations of LAD flow compared to data. Because the parametric identification from the zero-flow pressure experiments yields different optimal parameter values for each individual animal, and because the conscious exercise experiments were conducted on different animals and under different experimental conditions, a subset of parameters was identified to adjust to match the conscious state data. The model formulation is validated by showing that the model formulation using the top-ranked metabolic mechanism is able to match the conscious state data markedly better than lower ranked models.

To simulate myocardial perfusion *in vivo*, the two model components are simulated iteratively until they reach convergence. The measured aortic and left ventricular pressure data are inputs to Model 1 for a given set values of resistance vessel parameter values, C_{11} , C_{12} and C_{13} , representing vessel tones in the three myocardial layers. The predicted flow from Model 1, along with the given measured heart rate and estimated $M\dot{V}_{O_2}$, is used to compute the metabolic signal for use with Model 2. Model 2 is simulated to estimate the vessel diameters in each layer, from which the average resistances and compliances are computed:

$$\bar{R}_j = \left(\frac{V_0}{C_{1j}\bar{p}_{tm,j} + V_0} \right)^2 R_0 \approx \left(\frac{V_0}{C_{1j}\bar{p}_{tm,j} + V_0} \right)^2 R_0 \Rightarrow C_{1i} = \frac{\sqrt{\frac{R_0}{\bar{R}_j}} V_0 - V_0}{\bar{P}_{tm,j}} \quad (34)$$

The computed compliance values are fed back into Model 1, and the iterative process is carried out until

Models 1 and 2 agree and the predicted haemodynamic state reaches convergence.

To calibrate the model to simulate exercise, we perform the following analysis to identify a set of adjustable parameters that satisfy two criteria: (1) parameters in the set are estimated from the zero-flow pressure experiments with a relatively high degree of uncertainty and (2) simulations of *in vivo* myocardial perfusion are sensitive to the values of parameters in the set of identified parameters.

The uncertainty of the values estimated from the zero-flow pressure experiments is quantified based on the coefficient of variation *CoV*:

$$CoV(\theta) = 100 \frac{\sigma(\theta)}{\mu(\theta)} \quad (35)$$

where σ and μ are the SD and average of parameter θ used in Model 2. Next, we calculate parameter sensitivities using rest and exercise simulations (Pradhan *et al.* 2016):

$$X_i(\theta) = \frac{10}{\mathbf{p}_i(\theta)} \left| \mathbf{p}_i(\theta + 0.1\theta) - \mathbf{p}_i(\theta) \right| \quad (36)$$

where prediction vectors \mathbf{p}_i are simulation results; $\mathbf{p}_1 = F_{rest}(t)$, $\mathbf{p}_2 = F_{exer.}(t)$, $\mathbf{p}_3 = (ENDO/EPI)_{rest}$, $\mathbf{p}_4 = (ENDO/EPI)_{exer.}$ correspond to flow and ENDO/EPI flow ratio in rest and exercise. The sensitivity index X_i represents the ratio of change in error relative to a change in parameter value. For example, a sensitivity value of 1 means 1% change in parameter corresponds to 1% change in the model prediction. Finally, the overall model sensitivity S to each parameter is computed as the sum of sensitivities associated with each of the four predictions:

$$S(\theta) = \sum_i \|X_i(\theta)\| \quad (37)$$

To find the set of adjustable parameters, we find the parameters θ with $CoV(\theta) > 30\%$ and $S(\theta) > 0.1$. To estimate the parameters, we define model residual errors as:

$$\begin{aligned} r_r(t_k) &= \frac{F_{rest}(t_k) - F_{rest}^{data}(t_k)}{F_{rest}^{data}(t_k)}, \\ r_e(t_k) &= \frac{F_{exer.}(t_k) - F_{exer.}^{data}(t_k)}{F_{exer.}^{data}(t_k)} \end{aligned} \quad (38)$$

where F_{rest}^{data} and $F_{exer.}^{data}$ are LAD flow data in rest and exercise. Then, the cost function for the parameter estimation is

$$E_3 = w_f (\mathbf{r}_r^T \mathbf{r}_r + \mathbf{r}_e^T \mathbf{r}_e) + w_e |(ENDO/EPI)_{rest} - 1.25| \quad (39)$$

with weights w_f and w_e .

Results

Model 1 identification

Figure 1 shows an example data set for the zero-flow pressure experiment along with a fit of Model 1 for an individual animal under control conditions. The top two rows show the pressure tracings at different levels of CPP. At roughly $t = 7$ s, the LAD flow is occluded and the decay of pressure at a distal site is recorded for ~ 4 s. The bottom panels in Fig. 1 show data and model predictions of average flow and ENDO/EPI flow ratio measured before the occlusion. Model fits to the zero-flow pressure time course data for all animals and experimental conditions are provided in the Supporting information (Figs S2 to S13).

Figure 4 shows the measured and model-predicted total flow data for the four individual pigs for the three different experimental preparations. In control and haemodilution conditions, flow is maintained at roughly constant values over an autoregulatory range of CPP values between 60 and 120 mmHg. The total flow is elevated in haemodilution compared to the control to maintain oxygen delivery. Infusion of dobutamine significantly increases the flow compared to the control and haemodilution conditions and tends to abolish the autoregulatory response in all animals.

The Model 1 fits yield estimates of resistance vessel diameter at each CPP level under each experimental condition for each animal. These diameter estimates are illustrated in Fig. 3 for all three experimental conditions for the midwall layer for one experimental animal. Analogous predictions for all myocardial layers and for all animals are plotted are provided in the Supporting information (Figs S14 to S25).

Model 2 (representative vessel model) identification

Model 1 fits to the zero-flow pressure data are analysed using Model 2 to determine whether and how the competing versions of the representative vessel model are able to capture the *in vivo* autoregulatory behaviour underlying the zero-flow pressure dynamics. As illustrated in Fig. 3A (as well as in the Supporting information, Figs S14 to S25), Model 1 yields estimates of resistance vessel diameter as functions of transmural vessel pressure for three different experimental conditions, for three myocardial layers and for four individual animals at each of six values of CPP. Each of the seven competing versions of Model 2 (representing different formulations of the metabolic mechanism) are fit to this data set to determine the most probable model best able to represent the data. Example fits, associated with the flow-times- $M\dot{V}_{O_2}$ metabolic mechanism, are shown in Fig. 3A.

Table 3. Models are ordered by their $AICc_k$ value with the best model ranked 1

| Metabolic signal # | Metabolic signal | $AICc_k$ | Δ_k | RL_k | Rank |
|--------------------|---|----------|------------|------------------------|------|
| 6 | $F \cdot M$, flow times $M\dot{V}_{O_2}$ | 542 | 0 | 1.00 | 1 |
| 5 | $F \cdot \Delta S$, flow times oxygen extract. | 556 | 14 | 2.86×10^{-2} | 2 |
| 2 | $M\dot{V}_{O_2}$, metabolic rate | 610 | 68 | 4.66×10^{-8} | 3 |
| 3 | S_v , venous oxygen saturation | 614 | 72 | 1.68×10^{-8} | 4 |
| 4 | LS_v , Regionally varying S_v | 617 | 75 | 8.14×10^{-9} | 5 |
| 1 | ATP, ATP release from RBC's | 627 | 85 | 5.62×10^{-10} | 6 |
| 7 | $M\dot{V}_{O_2}^2$, non-linear metabolic | 688 | 146 | 1.50×10^{-16} | 7 |

Table 3 lists the estimated $AICc_k$, Δ_k , and RL_k values for the seven models, illustrating that the flow-times- $M\dot{V}_{O_2}$ metabolic mechanism is the highest ranked model, identified as the maximally probable among the models tested.

Figure 3 also plots the regulatory signals predicted by the model for the fits to the midwall myocardial layer show in Fig. 3A. For all three experimental conditions, the resistance vessel constricts with increasing the transmural pressure. In control and haemodilution conditions, the total activation level A steadily increases from 0 for low CPPs (full dilatation) to 0.8–0.9 for high CPPs. With the addition of dobutamine, the overall activation is shifted down. Figure 3C–E shows the variation of each mechanism in response to changes in CPP and experimental conditions. The myogenic contribution increases with increasing the transmural pressure, with the greatest values in the haemodilution + dobutamine case. The predicted autonomic contribution is almost constant over the observed range of CPP because the

heart rate is almost constant for each experimental condition. The autonomic contribution is elevated in the haemodilution + dobutamine case as a result of a higher the heart rate for this condition compared to other cases.

The metabolic signal is predicted to be an order of magnitude smaller than the myogenic and autonomic signals for the midwall layer for this animal under these conditions. Figure 3C shows that the strongest contributor to the pressure autoregulatory response is the myogenic mechanism, with S_{myo} increasing from 0 at the lowest CPP to 8 at the CPP = 140 mmHg (corresponding to the average transmural pressure of ~60 mmHg in the midwall region). The autonomic signal makes the biggest contribution to increasing diameter under haemodilution + dobutamine compared to other cases. This prediction is similar to that of Pradhan *et al.* (2016), who predicted that the open-loop autonomic signal contributes more to the response in coronary flow to increasing demand in exercise than the metabolic feedback signal.

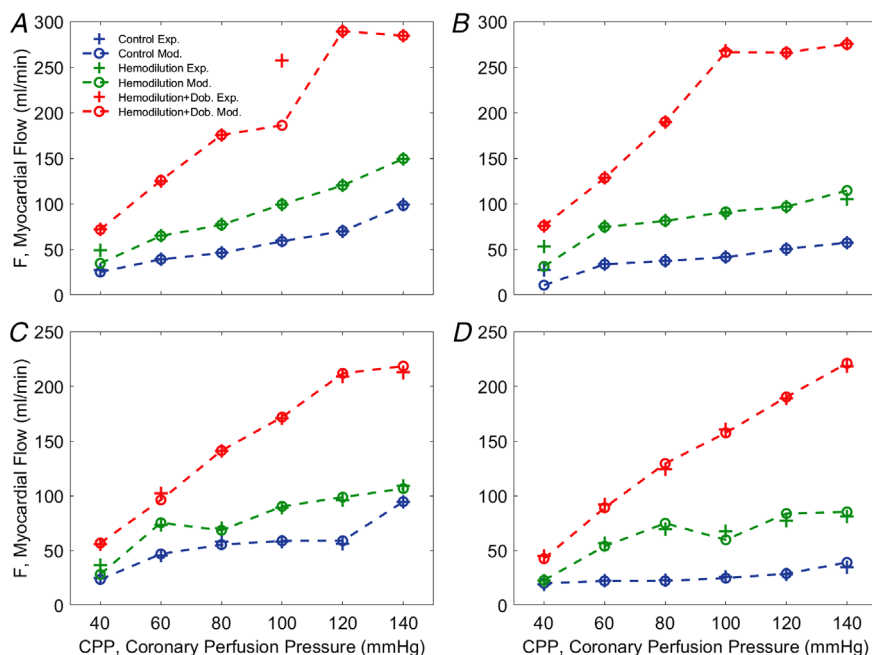


Figure 4. Measured vs. model-predicted LAD flow for each of four experimental animals under three different experimental conditions

Each panel (A–D) plots model simulations compared to data from one of four individual animals. In control and haemodilution conditions, coronary autoregulation impedes a significant increase in flow with increases in CPP (60–120 mmHg). However, the overall myocardial blood flow is elevated with haemodilution. Dobutamine infusion significantly increases the flow compared to the control and haemodilution conditions and largely abolishes the autoregulatory response in all animals. [Colour figure can be viewed at wileyonlinelibrary.com]

Figures 5, 6 and 7 illustrate how the predicted resistance vessel diameters and regulatory signals vary with CPP in each layer of the myocardium, summarizing predictions for all experimental animals. In the subepicardium (Fig. 5), the diameter decreases with increasing CPP under all experimental conditions. This trend is reversed in the subendocardium (Fig. 7), where an increase in vasodilatation with increasing perfusion pressure counters the action of increasing transmural pressure. In the haemodilution + dobutamine experiments, in particular (Fig. 7B), the subendocardium is predicted to be almost fully vasodilated across all values of CPP.

As expected, the myogenic mechanism (Figs 5C, 6C and 7C), makes the greatest contribution to the pressure autoregulatory response in the subepicardium, and smaller contributions in the midwall and sub-endocardial layers. The autonomic signal contribution (Figs 5D, 6D and 7E) is not predicted to vary substantially with CPP, indicating that this signal does not represent an important factor in eliciting the pressure autoregulation response simulated here. This prediction is expected because heart rate does not substantially change with CPP in these experiments. Thus, we conclude that sympathetic outflow to vascular smooth muscle also does not substantially change with CPP in these experiments. However, the baseline of the autonomic signal increases from the subepicardium to the sub-

endocardium, indicating that the subendocardium may be more sensitive to changes in sympathetic tone than the other layers.

In all layers, the metabolic signal (Figs 5E, 6E and 7E) is predicted to make a far greater contribution to the vasoregulation in the haemodilution + dobutamine case compared to the other experimental conditions. In all layers, the metabolic signal tends to increase with CPP, and tends to be slightly greater under haemodilution conditions compared to control. The magnitude of the increase with CPP is greatest for the haemodilution + dobutamine case because the oxygen demand is greatest in this condition.

Model validation: simulating exercise

The ability of the top performing metabolic signal model, *F-M*, is validated by evaluating its ability to simulate coronary flow regulation in conscious resting vs. exercise conditions. Figure 8 shows input data on aortic and left-ventricular pressures obtained under resting (Fig. 8 left panel) and moderate treadmill exercise (2–4 mph, 0% grade) (Fig. 8 right panel). These pressure data are used to drive the model to match the measured LAD flows illustrated in Fig. 9.

Under resting conditions, the animal’s heart rate was observed to be 84 beats min⁻¹, with systolic and diastolic

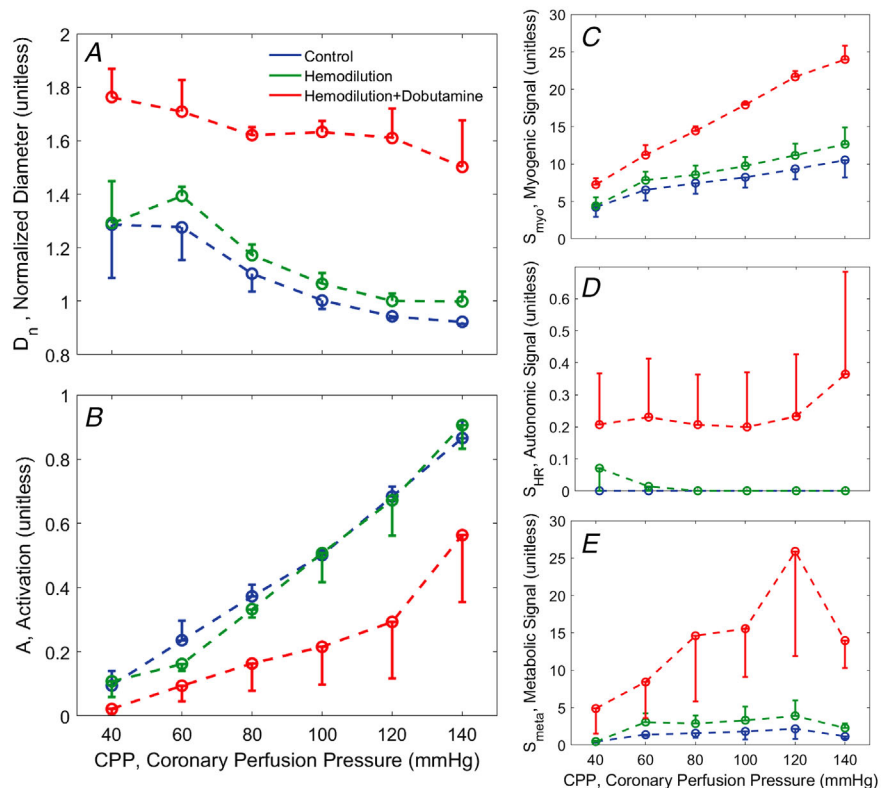


Figure 5. Vasoregulation in subepicardial vessels
 A, predicted mean ± SE of subepicardial resistance vessel diameter is plotted as a function of CPP. B, predicted mean ± SE of total vessel activation is plotted as a function of CPP. C, predicted mean ± SE of myogenic activation signal is plotted as a function of CPP. D, predicted mean ± SE of autonomic activation signal is plotted as a function of CPP. E, predicted metabolic activation signal is plotted as a function of CPP. [Colour figure can be viewed at wileyonlinelibrary.com]

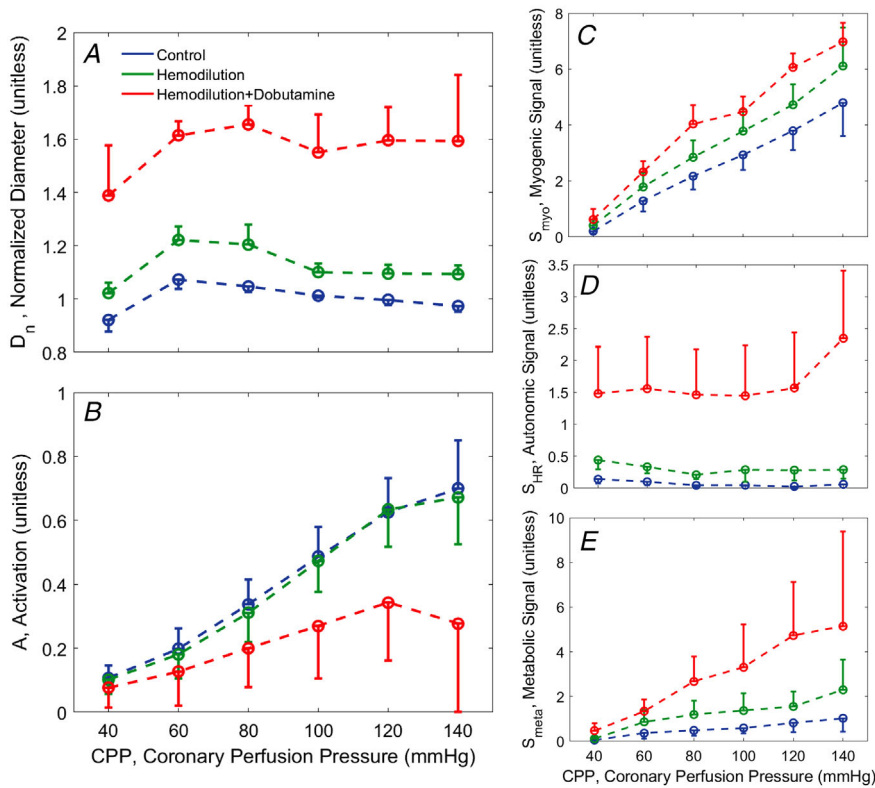


Figure 6. Vasoregulation in midwall vessels
 A, predicted mean \pm SE of subepicardial resistance vessel diameter is plotted as a function of CPP. B, predicted mean \pm SE of total vessel activation is plotted as a function of CPP. C, predicted mean \pm SE of myogenic activation signal is plotted as a function of CPP. D, predicted mean \pm SE of autonomic activation signal is plotted as a function of CPP. E, predicted metabolic activation signal is plotted as a function of CPP. [Colour figure can be viewed at wileyonlinelibrary.com]

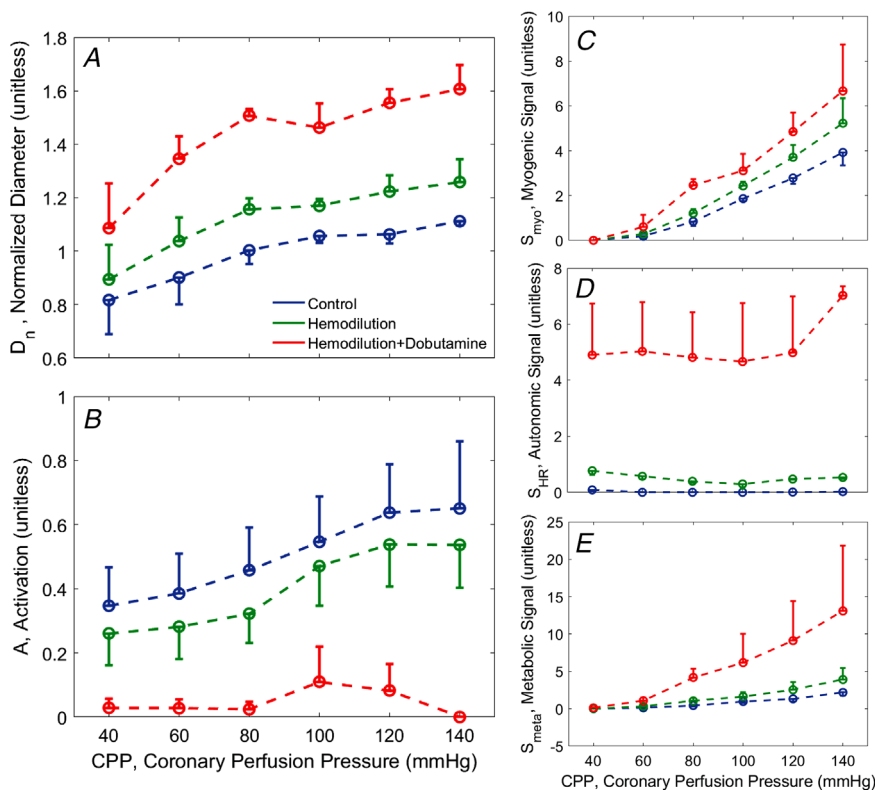


Figure 7. Vasoregulation in subendocardial vessels
 A, predicted mean \pm SE of subepicardial resistance vessel diameter is plotted as a function of CPP. B, predicted mean \pm SE of total vessel activation is plotted as a function of CPP. C, predicted mean \pm SE of myogenic activation signal is plotted as a function of CPP. D, predicted mean \pm SE of autonomic activation signal is plotted as a function of CPP. E, predicted metabolic activation signal is plotted as a function of CPP. [Colour figure can be viewed at wileyonlinelibrary.com]

aortic pressures of ~149 and 102 mmHg, with developed pressure in the ventricle matching peak systolic aortic pressure. During exercise, the heart rate increases to 114 beats min⁻¹ and aortic pressures increase to 162 and 118 mmHg. We assume a resting average myocardial oxygen consumption rate of 60 μL O₂ min⁻¹ g⁻¹ based on Kiel *et al.* (2018). Based on the observed aortic pressures and heart rates, we estimate that left-ventricular mechanical power output increases by 32% in exercise compared to control (Holmberg *et al.* 1971). Furthermore, based on the expected linear scaling of power output and oxygen demand, we approximate the exercise oxygen consumption rate to be 79.2 μL O₂ min⁻¹ g⁻¹ in exercise.

Given the measured driving pressures and the estimated myocardial oxygen consumption rates, the integrated model can be used to simulate myocardial perfusion in resting and exercise conditions. However, parameters estimated based on the zero-flow pressure experiments (Tables 1 and 2) show a degree of variability and

uncertainty. Moreover, they are estimated for different individual animals. Thus, to match the conscious data of Figs 8 and 9, a subset of adjustable parameters was identified, as described in the methods. Adjustable parameters for the conscious experiments are listed in Table 4.

Simulated total LAD flow, obtained using the identified *F-M* model, was compared with measured data for baseline rest (Fig. 9A) and exercise (Fig. 9C) conditions. The model effectively captures both the pulsatile nature of the flow and the dynamics of flow recruitment in exercise. Figure 9B,C shows the predicted flow to each of the three myocardial layers, revealing that the subendocardial flow is positive only during diastole, and becomes negative during systole. By contrast, the subepicardial flow shows positive peaks during both systole and diastole. During exercise, when the driving aortic systolic pressure increases, the systolic peak becomes more important in the subepicardium.

Figure 8. Aortic and left-ventricular pressure time courses
Measured aortic and left-ventricular pressure time courses for a conscious pig in rest (left) and exercise (right). [Colour figure can be viewed at wileyonlinelibrary.com]

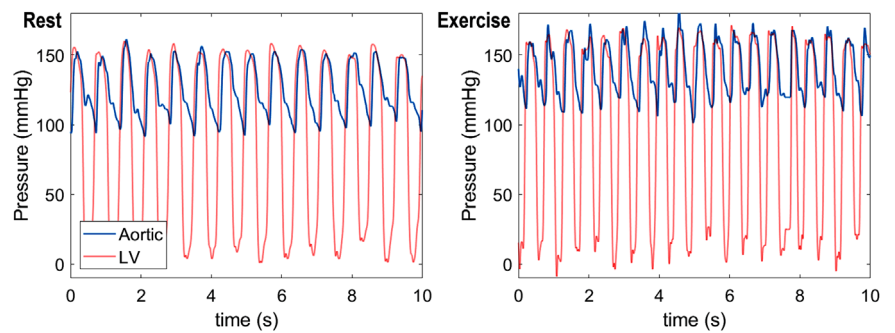


Figure 9. Coronary flow dynamics in rest vs. exercise
A, model-predicted total LAD flow under resting control conditions is compared with the measured flow. B, predicted contributions of subendocardial, midwall and subepicardial flow to total LAD flow under resting conditions are shown. C, model-predicted total LAD flow under exercise conditions is compared with the measured flow. D, predicted contributions of subendocardial, midwall and subepicardial flow to total LAD flow under exercise conditions are shown. In both rest and exercise conditions the model simulations reflect the integrated model using the top-ranked using the *F-M*, flow times $M\dot{V}_{O_2}$, metabolic signal. [Colour figure can be viewed at wileyonlinelibrary.com]

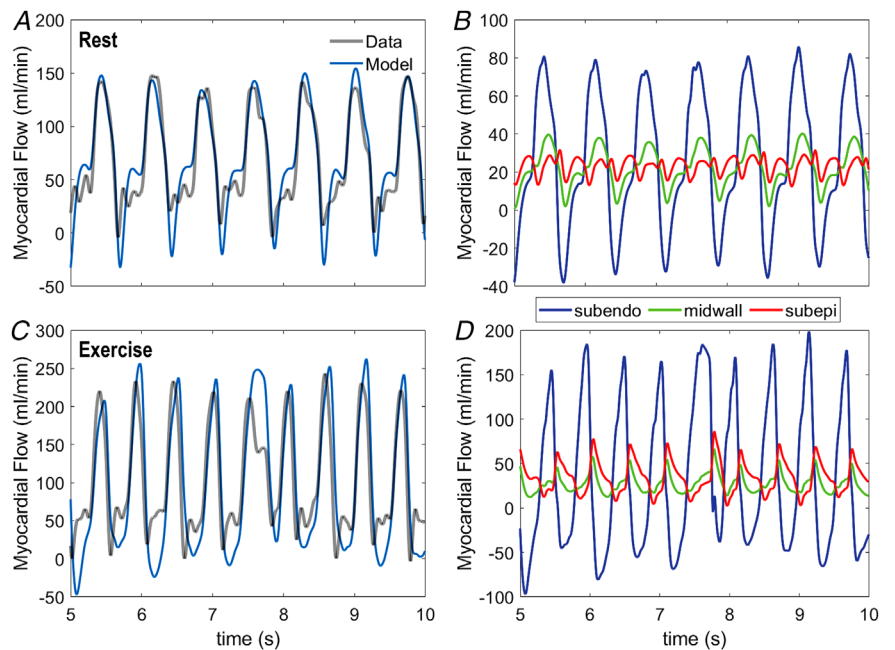


Table 4. List of adjustable parameters and estimated values for *in vivo* simulations

| Parameter | Layer | CoV | Sensitivity | Estimated value |
|-----------|---------------|--------|-------------|-----------------|
| ϕ_m | Midwall | 0.3084 | 1.38 | 133.577 |
| C_{myo} | Midwall | 0.3075 | 0.13 | 13.923 |
| C_0 | Midwall | 0.3405 | 2.07 | -3.296 |
| ϕ_p | Subepicardial | 7.6885 | 0.29 | 20.736 |
| ϕ_m | Subepicardial | 0.3633 | 2.53 | 75.439 |
| C_m | Subepicardial | 0.5246 | 1.32 | 107.652 |
| C_{myo} | Subepicardial | 0.3010 | 0.28 | 27.483 |
| C_0 | Subepicardial | 0.5264 | 0.46 | -9.735 |

Model predictions of average flow and of the subendocardial-to-subepicardial perfusion ratio are compared with experimental data in Fig. 10. In fitting the flow data, the model correctly predicts the transmural variations in perfusion in rest vs. exercise. For comparison, predictions associated with the best fit of the MS_{LSv} (ranked 5 in Table 3) model are shown in Fig. 10A,B. This model is able to match the measured flow but, in doing so, predicts subendocardial-to-subepicardial perfusion ratios that are much lower than physiological. These results represent a validation of our identified model and of our model selection procedure. Moreover, the modelling framework provides predictions of transmural constriction/dilatation of vessels in terms of their overall vascular tone (e.g. activation A), and normalized diameter (Fig. 10C,D). Subendocardial layer tone is predicted to decrease to almost full vasodilatation in exercise, whereas the subepicardial layer tone increases. The overall increase in tone in the subepicardial layer is overcome by the pressure-induced dilatation (Fig. 10D).

Figure 11 illustrates how each regulatory signal contributes to the overall predicted response to exercise

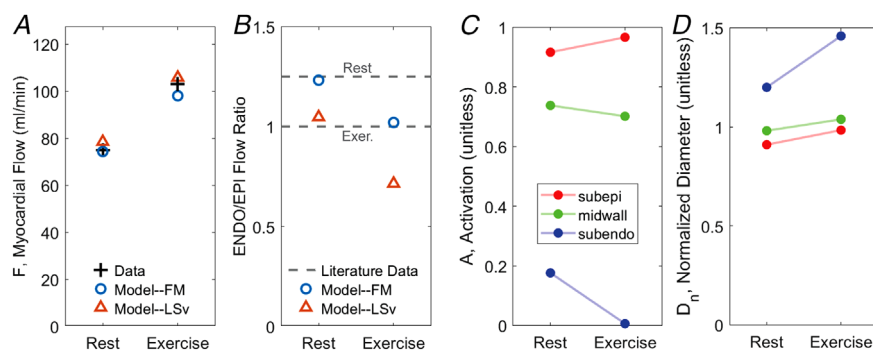
by showing the exercise-induced change in each stimuli ($\Delta S = S_{tone}^{exercise} - S_{tone}^{rest}$) in each layer of the myocardium for the $F\text{-}M$ model. The model-predicted vasoconstriction in the subepicardium in exercise is shown to be a myogenic response to elevated perfusion pressure. The autonomic vasodilatation signal (S_{HR}) is predicted to preferentially influence the subendocardium, with a negligible effect on the subepicardium.

Discussion

The physiological balance between coronary blood and myocardial oxygen consumption ($M\dot{V}_{O_2}$) is preserved over a variety of physiological and pathophysiological conditions, including in the response to exercise where increases in oxygen demand are met by corresponding increases in oxygen delivery.

Modelling framework and the overall approach

The present study integrates a lumped approach to simulating ventricular-vascular interaction and myocardial perfusion adapted from Spaan *et al.* (2000), Mynard *et al.* (2014) and Mynard & Smolich (2016), a vasoregulation model adapted from Carlson and Secomb (2005), and a panel of competing mechanisms representing metabolic control of myocardial blood flow. The multiscale modelling framework is illustrated in Fig. 2. The model components are identified based on analysis of data from zero-flow pressure experiments, as illustrated in Fig. 1. Based on their relative ability to match the experimental data, ranked based on goodness of fit and degrees of freedom in the models, the maximally probable metabolic mechanism is identified, and further validated based on simulations of conscious response to exercise (Figs 8, 9 and 10). One of the major novelties of the present study is the application of established tools for

**Figure 10.** Regulation of coronary flow in exercise

A, comparison of measured to model-predicted total LAD flow in resting vs. exercise conditions. B, comparison of measured to model-predicted subendocardial-to-subepicardial (ENDO/EPI) flow in resting vs. exercise conditions. In (A) and (B), fits from a competing metabolic model are illustrated, showing that the lower ranking model fails to capture the ENDO/EPI flow ratio. C, predicted total vascular tone activation in each layer of the myocardium for resting and exercise conditions. D, predicted representative resistance vessel diameter in each layer of the myocardium for resting and exercise conditions. [Colour figure can be viewed at wileyonlinelibrary.com]

model discrimination in the context of multiscale systems with high degrees of uncertainty and structural and parametric freedom.

Identification of hypothetical metabolic signal

Data from three conditions and four experimental animals were analysed with model formulations that integrated seven competing hypotheses for the nature of the metabolic feedback signal. The competing hypotheses are summarized in Table 3, along with a summary ranking of most-to-least probable mechanism. These results illustrate a combined structural and parametric model identification, with several competing models ruled out as not viable. In the top-ranked model, the metabolic signal is represented as proportional to metabolic rate and flow. Our preliminary interpretation of this result is that it represents an ephemeral metabolic signal for which production is proportional to $M\dot{V}_{O_2}$ and delivery is proportional to flow. Potential candidates for such a signal include short-lived reactive species such as H_2O_2 (Saitoh *et al.* 2006).

Predicted resistance vessel diameters are plotted as functions of transmural pressure at different CPP values for the midwall layer in one experimental animal in Fig. 4. Predicted diameters are plotted as functions of CPP for all animals under all conditions in the Supporting information (Figs S14 to S25). Simulations

consistently show a greater resistance vessel diameter for the haemodilution compared to the control case. These differences are small but important because they are consistently required to match the data on flow and pressure. Indeed, the reason why the ATP-mediated metabolic model (Metabolic Signal #1) (Table 3) cannot effectively match data from the zero-flow pressure experiment is that it cannot capture this phenomenon. In other words, even with arbitrarily adjusting parameters, the output of the model capturing the ATP hypothesis cannot be made consistent with the observed pressure response to upstream occlusion. Therefore, by combining the lumped microcirculation model, a simple vessel mechanics model and our ATP-mediated metabolic control model to analyse these data, our analysis argues against the hypothesis that ATP derived from red blood cells represents the primary metabolic signal for coronary blood flow regulation. Rigorously, discarded models are judged as non-viable only in the form that they are implemented for this analysis. Nevertheless, this finding highlights the type of novel insight that comes from analysing time-dependent data using even a relatively crude multiscale and spatially distributed modelling framework.

Thus, although we do not interpret the top-ranked model as 'proven' or 'correct', the disproof of the alternatives usefully narrows the scope of possibilities. Furthermore, even if the basic formulation of the *F·M* model correctly represents the basic action of metabolic mechanism, this analysis does not identify the molecular mechanism underlying the putative mechanism. Rather, we interpret the ephemeral metabolic signal *F·M* model as a working hypothesis to test and refine with further experiments and models that represent the metabolic and signalling mechanisms with more mechanistic resolution. The validity of this working hypothesis is supported by the ability of the associated model to simulate the response in myocardial perfusion to exercise.

Matching demand in exercise

The ability of the ephemeral signal hypothesis, when integrated in this modelling framework, to effectively simulate the dynamics of myocardial perfusion in the transition from resting state to exercise is illustrated in Figs 8, 9 and 10. Because lower-ranked models (e.g. Metabolic Signal #5) predict a greater than physiological drop in subendocardial perfusion with exercise, these results represent a validation of the maximal-likelihood evaluation process: the top-ranked model captures behaviour not used for identification, whereas lower ranked models fail.

Simulation of the exercise response also yields novel hypotheses regarding the regional response to increasing exercise demand. For example, simulations predict that

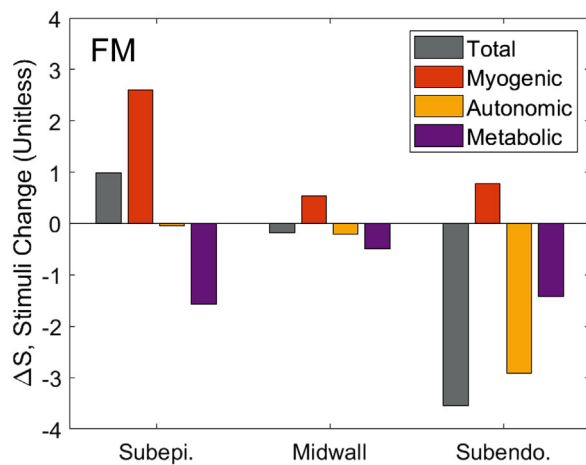


Figure 11. The change in total, myogenic, metabolic and autonomic stimuli in response to exercise

The grey bars show the net total change in stimulus in each layer exercising compared to rest conditions. The individual contributors to the stimuli signal—myogenic, autonomic and metabolic—sum to the total in each layer. The total stimulus in the subepicardium is higher in exercise than in rest, resulting in an increased activation. The primary contributor to the increased activation in the subepicardium in exercise is the myogenic stimulus. In the subendocardium, exercise causes an overall reduction in vascular tone, as a result of a combination of metabolic and autonomic stimuli. [Colour figure can be viewed at wileyonlinelibrary.com]

subepicardial vascular tone is higher during exercise than at rest, as a result of a myogenic response to elevated perfusion pressure. Another prediction associated with the exercise simulations is that sympathetic-mediated vasodilatation preferentially influences the sub-endocardium. The physiological role of sympathetic activation in the control of myocardial perfusion is much more complex than the simplified way it is treated in the current model, which does not take into account a potentially heterogeneous distribution of α -mediated constriction effectors (Duncker & Bache, 2008; Goodwill *et al.* 2017). Moreover, measurements of β_2 -adrenergic receptor densities show transmurally uniform expression in the human myocardium (Murphree & Saffitz, 1989; Beau *et al.* 1993). Furthermore, subepicardial resistance arterioles from pig have been observed to show a greater vasodilatation response to selective β_2 stimulation and to have greater β_2 receptor density than subendocardial resistance arterioles (Hein *et al.* 2004). At the same time, there is evidence suggesting that α -mediated vasoconstriction acts to preferentially distribute flow to the subendocardium during exercise (Huang & Feigl, 1988; Morita *et al.* 1997). However, this maintenance of ENDO/EPI ratio appears to occur under conditions in which heart rate (≥ 240 beats min^{-1}) and $M\dot{V}_{\text{O}_2}$ ($> 500 \mu\text{L O}_2 \text{ min}^{-1} \text{ g}^{-1}$) are very high because alternative studies at lower levels of exercise have failed to support the preferential redistribution of blood flow toward the endocardium under normal physiological conditions (Gwartz *et al.* 1992; Baumgart *et al.* 1993). Regardless, it is apparent that α -constriction does facilitate this redistribution of coronary flow in the setting of ischaemia (Nathan & Feigl, 1986; Chilian & Ackell, 1988). Our model lumps α - and β -mediated effects on resistance vessels into a single signal, S_{HR} . Thus, the model prediction that the gain associated with this signal is greater in the subendo- compared to subepicardium is consistent with the interpretation that the overall response to sympathetic stimulation is relatively more vasodilatory in the sub-endocardium compared to the subepicardium. Moreover, this overall transmural gradient in the response of vascular tone in exercise is undoubtedly influenced by regional heterogeneities in responses of vessels of different sizes and transmural depth to metabolic, myogenic and autonomic signals. A deeper investigation of how these factors work together *in vivo* may be possible by combining models with more anatomically resolved detail (Namani *et al.* 2020) with the regulatory mechanisms analysed in the present study.

Limitations of the study

The current model uses a simplified lumped-parameter of myocardial circulation downstream of the LAD,

capturing regional differences in perfusion only in terms of a relatively coarse representation of transmural heterogeneity in the LV free wall. Previous applications of this approach have coupled the myocardial perfusion model to a 1D haemodynamics models of epicardial vessels to simulate regional perfusion; for example, in the left-ventricular free wall *vs.* the septum (Mynard *et al.* 2014; Mynard & Smolich, 2016). Moreover, the target transmural flow distribution (ENDO/EPI ratio) in the present study is estimated from literature reports, which consistently report ENDO/EPI at only one experimental point (control, CPP = 100 mmHg). More data on variation of transmural perfusion with CPP would be valuable in constraining and testing model behaviour. More broadly, a rigorous uncertainty quantification will be useful in analysing measurement errors propagated to the final model predictions. Finally, the current model assumes the intramyocardial pressure is a linear function of left ventricular pressure in all cases. This assumption has to be re-examined especially for dobutamine experiments that involve elevations in the myocardial contractility, which directly influences the intramyocardial pressure via changes in the myocyte shortening induced pressure (Algranati *et al.* 2010).

Finally, although our analysis points to a single candidate mechanism as representing the metabolic signalling pathway for control of myocardial perfusion, it is possible and even probable that multiple different specific mediators operate under the aegis of this general framework. Moreover, the analysis conducted here is limited to considering each putative metabolic mechanism on its own and does not rule out the possibility of multiple mechanisms acting in parallel. Most concretely, this analysis reveals which of the tested mechanisms are unable to effectively explain the observed *in vivo* autoregulatory behaviour, and does not unambiguously identify the correct mechanism that is operative *in vivo*. How coronary perfusion is regulated to be directly proportional to oxygen demand is a fundamental question in coronary physiology. The general framework that survives testing against these data explicitly invokes a direct proportionality between a vasodilatory signal and oxygen consumption rate. Thus, this framework may ultimately prove to be a convenient temporary placeholder against which to judge more detailed specific hypotheses. Alternatively, it may prove to be the mechanistically correct foundation on which to build more detailed specific hypotheses.

References

- Algranati D, Kassab GS & Lanir Y (2010). Mechanisms of myocardium-coronary vessel interaction. *Am J Physiol Heart Circ Physiol* **298**, H861–H873.

- Bassingthwaight JB, Beard DA & Li Z (2001). The mechanical and metabolic basis of myocardial blood flow heterogeneity. *Basic Res Cardiol* **96**, 582–594.
- Baumgart D, Ehring T, Kowallik P, Guth BD, Krajcar M & Heusch G (1993). Impact of alpha-adrenergic coronary vasoconstriction on the transmural myocardial blood flow distribution during humoral and neuronal adrenergic activation. *Circ Res* **73**, 869–886.
- Beau SL, Tolley TK & Saffitz JE (1993). Heterogeneous transmural distribution of beta-adrenergic receptor subtypes in failing human hearts. *Circulation* **88**, 2501–2509.
- Berwick ZC, Dick GM, Moberly SP, Kohr MC, Sturek M & Tune JD (2012). Contribution of voltage-dependent K⁺ channels to metabolic control of coronary blood flow. *J Mol Cell Cardiol* **52**(4), 912–919. <https://doi.org/10.1016/j.yjmcc.2011.07.004>
- Breisch EA, White FC, Nimmo LE & Bloor CM (1986a). Cardiac vasculature and flow during pressure-overload hypertrophy. *Am J Physiol* **251**, H1031–H1037.
- Breisch EA, White FC, Nimmo LE, McKirnan MD & Bloor CM (1986b). Exercise-induced cardiac hypertrophy: a correlation of blood flow and microvasculature. *J Appl Physiol* (1985) **60**, 1259–1267.
- Carlson BE, Arciero JC & Secomb TW (2008). Theoretical model of blood flow autoregulation: roles of myogenic, shear-dependent, and metabolic responses. *Am J Physiol Heart Circ Physiol* **295**, H1572–H1579.
- Carlson BE & Secomb TW (2005). A theoretical model for the myogenic response based on the length-tension characteristics of vascular smooth muscle. *Microcirculation* **12**, 327–338.
- Chilian WM & Ackell PH (1988). Transmural differences in sympathetic coronary constriction during exercise in the presence of coronary stenosis. *Circ Res* **62**, 216–225.
- Dole WP & Nuno DW (1986). Myocardial oxygen tension determines the degree and pressure range of coronary autoregulation. *Circ Res* **59**, 202–215.
- Duncker DJ & Bache RJ (2008). Regulation of coronary blood flow during exercise. *Physiol Rev* **88**, 1009–1086.
- Goodwill AG, Dick GM, Kiel AM & Tune JD (2017). Regulation of coronary blood flow. *Compr Physiol* **7**, 321–382.
- Guiot C, Pianta PG, Cancelli C & Pedley TJ (1990). Prediction of coronary blood flow with a numerical model based on collapsible tube dynamics. *Am J Physiol* **258**, H1606–H1614.
- Gwartz PA, Dodd OJ, Downey HF, Mass HJ, Barron BA, Williams AG, Jr. & Jones CE (1992). Effects of a coronary alpha 1-constriction on transmural left ventricular flow and contractile function. *Am J Physiol* **262**, H965–H972.
- Hein TW, Zhang C, Wang W & Kuo L (2004). Heterogeneous beta2-adrenoceptor expression and dilation in coronary arterioles across the left ventricular wall. *Circulation* **110**, 2708–2712.
- Ho SY, Sanchez-Quintana D & Becker AE (2004). A review of the coronary venous system: a road less travelled. *Heart Rhythm* **1**, 107–112.
- Hoffman JI & Spaan JA (1990). Pressure-flow relations in coronary circulation. *Physiol Rev* **70**, 331–390.
- Holmberg S, Serzysko W & Varnauskas E (1971). Coronary circulation during heavy exercise in control subjects and patients with coronary heart disease. *Acta Med Scand* **190**, 465–480.
- Holtz J, Grunewald WA, Manz R, von Restorff W & Bassenge E (1977). Intracapillary hemoglobin oxygen saturation and oxygen consumption in different layers of the left ventricular myocardium. *Pflugers Arch* **370**, 253–258.
- Huang AH & Feigl EO (1988). Adrenergic coronary vasoconstriction helps maintain uniform transmural blood flow distribution during exercise. *Circ Res* **62**, 286–298.
- Kiel AM, Goodwill AG, Baker HE, Dick GM & Tune JD (2018). Local metabolic hypothesis is not sufficient to explain coronary autoregulatory behavior. *Basic Res Cardiol* **113**, 33.
- Krombach RS, Clair MJ, Hendrick JW, Mukherjee R, Houck WV, Hebbbar L, Kribbs SB, Dodd MG & Spinale FG (1999). Amlodipine therapy in congestive heart failure: hemodynamic and neurohormonal effects at rest and after treadmill exercise. *Am J Cardiol* **84**, 3L–15L.
- Morita K, Mori H, Tsujioka K, Kimura A, Ogasawara Y, Goto M, Hiramatsu O, Kajiji F & Feigl EO (1997). Alpha-adrenergic vasoconstriction reduces systolic retrograde coronary blood flow. *Am J Physiol* **273**, H2746–H2755.
- Murphree SS & Saffitz JE (1989). Distribution of beta-adrenergic receptors in failing human myocardium. Implications for mechanisms of down-regulation. *Circulation* **79**, 1214–1225.
- Mynard JP, Penny DJ & Smolich JJ (2014). Scalability and in vivo validation of a multiscale numerical model of the left coronary circulation. *Am J Physiol Heart Circ Physiol* **306**, H517–H528.
- Mynard JP & Smolich JJ (2016). Influence of anatomical dominance and hypertension on coronary conduit arterial and microcirculatory flow patterns: a multiscale modeling study. *Am J Physiol Heart Circ Physiol* **311**, H11–H23.
- Namani R, Lee LC, Lanir Y, Kaimovitz B, Shavik SM & Kassab GS (2020). Effects of myocardial function and systemic circulation on regional coronary perfusion. *J Appl Physiol* (1985) **128**, 1106–1122.
- Nathan HJ & Feigl EO (1986). Adrenergic vasoconstriction lessens transmural steal during coronary hypoperfusion. *Am J Physiol* **250**, H645–H653.
- Navakatikyan MA (2007). A model for residence time in concurrent variable interval performance. *J Exp Anal Behav* **87**, 121–141.
- Pradhan RK, Feigl EO, Gorman MW, Brengelmann GL & Beard DA (2016). Open-loop (feed-forward) and feedback control of coronary blood flow during exercise, cardiac pacing, and pressure changes. *Am J Physiol Heart Circ Physiol* **310**, H1683–H1694.
- Saitoh S, Zhang C, Tune JD, Potter B, Kiyooka T, Rogers PA, Knudson JD, Dick GM, Swafford A & Chilian WM (2006). Hydrogen peroxide: a feed-forward dilator that couples myocardial metabolism to coronary blood flow. *Arterioscler Thromb Vasc Biol* **26**, 2614–2621.
- Snyder GK (1971). Influence of temperature and hematocrit on blood viscosity. *Am J Physiol* **220**, 1667–1672.

- Spaan JA, Cornelissen AJ, Chan C, Dankelman J & Yin FC (2000). Dynamics of flow, resistance, and intramural vascular volume in canine coronary circulation. *Am J Physiol Heart Circ Physiol* **278**, H383–H403.
- Tune JD, Goodwill AG, Kiel AM, Baker HE, Bender SB, Merkus D & Duncker DJ (2020). Disentangling the Gordian knot of local metabolic control of coronary blood flow. *Am J Physiol Heart Circ Physiol* **318**, H11–H24.
- Vinnakota KC, Mitchell DA, Deschenes RJ, Wakatsuki T & Beard DA (2010). Analysis of the diffusion of Ras2 in *Saccharomyces cerevisiae* using fluorescence recovery after photobleaching. *Phys Biol* **7**, 026011.
- Vinten-Johansen J & Weiss HR (1980). Oxygen consumption in subepicardial and subendocardial regions of the canine left ventricle. The effect of experimental acute valvular aortic stenosis. *Circ Res* **46**, 139–145.
- Young JM, Choy JS, Kassab GS & Lanir Y (2012). Slackness between vessel and myocardium is necessary for coronary flow reserve. *Am J Physiol Heart Circ Physiol* **302**, H2230–H2242.

Additional information

Open research badges



This article has earned an Open Data badge for making publicly available the digitally-shareable data necessary to reproduce the reported results. The data is available at <https://github.com/beards-lab/Multiscale-Coronary-Flow-Control>.

Data availability statement

The data and computer codes that support the findings of this study are available from the corresponding author upon reasonable request.

Competing interests

The authors declare that they have no competing interests.

Author contributions

HG, CAF, JDT and DAB conceived the study design. HG and DAB developed the model. JDT provided the experimental data. HG, CAF, JDT and DAB were involved in data analyses, subsequent interpretation and drafting the article. All authors critically reviewed the article. All authors approved the final version of this article and agree to be accountable for all aspects of the work. All persons designated as authors qualify for authorship, and all those who qualify for authorship are listed.

Funding

This study was funded by NIH R01 HL139813.

Keywords

coronary blood flow, metabolic control, myocardial perfusion, myogenic control, oxygen transport

Supporting information

Additional supporting information can be found online in the Supporting Information section at the end of the HTML view of the article. Supporting information files available:

Peer Review History

Statistical Summary Document

Computer codes and Supp Figs S1–S25